Research Article

Rossana Dimitri*, Martina Rinaldi, Francesco Tornabene, and Francesco Micelli

Numerical study of the FRP-concrete bond behavior under thermal variations

https://doi.org/10.1515/cls-2022-0193
received March 19, 2023; accepted March 28, 2023

Abstract: In a context where daily and seasonal temperature changes or potential fire exposure can affect the mechanical response of structures strengthened with fiber-reinforced polymer (FRP) composites during their life cycle, the present work studies the bond behavior of FRP laminates glued to concrete substrates under a thermal variation. The problem is tackled computationally by means of a contact algorithm capable of handling both the normal and tangential cohesive responses, accounting for the effect of thermal variations on the interfacial strength and softening parameters, which defines the failure surface and post cracking response of the selected specimen. A parametric investigation is performed systematically to check for the effect of thermo-mechanical adhesive and geometrical properties on the debonding load of the FRP-to-concrete structural system. The computational results are successfully validated against some theoretical predictions from literature, which could serve as potential benchmarks for developing further thermo-mechanical adhesive models, even in a coupled sense, for other reinforcement-to-substrate systems, useful for design purposes in many engineering applications.

Keywords: concrete, debonding, fiber/matrix bond, FRP, high-temperature properties, interface, thermomechanics

1 Introduction

The increased sensitivity toward the conservation of heritage construction and civil infrastructures has favored the study of novel methodologies and the development of innovative materials for structural repair and retrofitting [1,2]. One of the most recent innovations in strengthening existing reinforced concrete (RC) structures is related to the use of composite materials. Among such innovative materials, fiber-reinforced polymer (FRP) composites have gained an increased interest among scientists in both the reinforcement and structural repair fields [3–6]. The structural compatibility between FRP laminates and concrete substrates can be assured by chemical bonding based on the use of adhesives. In this scenario, the bond between these materials becomes a controlling factor that governs the design of strengthening interventions. It is well known from the experimental literature, that Mode II debonding is the most common failure mode in structures strengthened with externally bonded FRP plates [7–9], such that different setup tests have been proposed by scientists to investigate the behavior of FRP-to-substrate bonded joints under a pure Mode II loading condition [10–24]. Among the most common standard tests from the literature, there is the single-lap shear test and/or the double-lap shear test to investigate the bond-slip behavior of specimens under quasi-static and monotonic loading conditions, along with the debonding load, the effective bond length, and the full-range bond behavior [25–38]. Based on the existing investigations on bonded joint tests, it is noteworthy that the mechanical properties of both concrete substrates and bonding adhesives can affect the shape of a bond-slip model to yield different representative categories, namely, the elastic brittle [10,26,39–42], the bi-linear [10,14,43–49], the elastic–plastic–brittle [41,50–53], the trapezoidal [2,54–57], the rigid-softening [10,39,41,45,46,58], and the nonlinear [12,14,29,31,34,47,59–63] models. At the same time, the maximum load seems to be almost unaffected by the bond-slip model, which describes the debonding failure process of specimens in terms of load–deflection response, as found in the study of Hart-Smith [64].

The study of adhesively bonded joints started in 1938 with the pioneering works by Volkersen [65] and Goland and Reissner [66], followed by the research of Hart-Smith [64,66]. In such works, the authors described the shear response of an adhesive layer as elastic–plastic or bilinearly elastic behavior before reaching the ultimate

* **Corresponding author: Rossana Dimitri,** Department of Innovation Engineering, School of Engineering, University of Salento, 73100, Lecce, Italy, e-mail: rossana.dimitri@unisalento.it
Martina Rinaldi, Francesco Tornabene, Francesco Micelli: Department of Innovation Engineering, School of Engineering, University of Salento, 73100, Lecce, Italy

strain, while investigating the effect of mutual interaction among fractures within an RC beam on its final debonding failure under a pure Mode II loading. Later on, a large variety of studies in the literature focused on the full-range load-slip deformation process and debonding mechanism of the FRP-to-concrete interface under a mechanical loading at room temperature. An analytical solution was proposed by Yuan *et al.* [41] to describe the full-range behavior of the FRP-to-substrate bonded joints by a bi-linear bond-slip model. The same study was conducted by Teng *et al.* [44], with the addition of a tensile force applied on the other end of the FRP sheet. Later, Chen *et al.* [58] employed a rigid-softening model to describe the same behavior of Yuan *et al.* [41]. A trapezoidal bond-slip model was applied by Fernando *et al.* [57] to find the full-range behavior of FRP-to-substrate bonded joints, starting from the study of a carbon-fiber-reinforced polymer (CFRP) applied on a steel structure and using a ductile nonlinear adhesive [54,56]. Besides, the exponential bond-slip model was used by Dai *et al.* [33] assuming an infinite bond length, while other forms of the same model were used by Biscaia *et al.* [42], Caggiano *et al.* [49], Zhou *et al.* [59], Cornetti and Carpinteri [60], and Yuan *et al.* [62]. All these works focused on the debonding behavior of FRP-to-substrate interfaces under a pure shear loading, without evaluating the possible effect of temperature on the interfacial response, as can occur for FRP-strengthened structures exposed to climate changes or fire. The experimental results from the literature indicated that thermal loading could induce two possible effects on the bond behavior of FRP-to-substrate interfaces, along with the stress transfer and load-bearing capacity in the strengthened system. The first effect relies on the thermal-induced property variations of the adhesives and adherends. As detailed in the study of Rabinovitch [67], such an effect is strictly related to the low glass transition temperature (T_g) of ambient-cured bonding adhesives. For service temperatures higher than T_g, the adhesive transfers from a glassy state to a rubbery one, with a consecutive degradation of its stiffness and strength, along with an overall reduction of the stress interfacial transfer and premature debonding failure of the reinforcement laminate [23,67]. The second effect, instead, is related to a thermal incompatibility between the FRP and substrate, featuring different coefficients of thermal expansion that yield a thermal stress state. More specifically, the FRP thermal expansion in the longitudinal direction can be significantly different from the thermal expansion of the concrete substrate. This difference generates a thermal stress state with a meaningful influence on the bond interfacial strength and the mechanical stress state. Among different bonded joint tests, the most commonly used for experimental investigations about the thermomechanical bond behavior of FRP-to-concrete or FRP-to-steel interfaces rely on single-lap and double-lap shear tests under different thermal conditions [68–74].

Since the temperature variation affects both the interfacial stress state and material properties of the adhesive, temperature-dependent interfacial bond-slip models must be properly defined to account for any possible co-presence of interfacial thermal stresses and/or temperature-induced material property variation. In different shear test investigations from literature, these thermal stresses are ignored [71,75]. In the work by Hart-Smith [64], a double-lap joint was loaded both mechanically and thermally, to check for the solution of the interfacial problem in terms of ultimate load instead of a full-range debonding process, based on an elastic–plastic or bilinear-elastic behavior assumption, before the ultimate strain. An analytical solution was proposed by Gao *et al.* [76], based on a bi-linear bond-slip model, for the study of the full-range behavior of FRP-to-concrete bonded joints under Mode II thermo-mechanical loading. Their theoretical results indicated that the debonding load was highly affected by thermal stresses, making it possible to isolate them from each other. It was also found that Mode II debonding load can be influenced by a varying service temperature. More recently, Gao *et al.* [77] have found some closed-form analytical solutions for further bond-slip models while analyzing the influence of the bond-slip shape and bond length on both the stress transfer mechanism and debonding process of FRP-to-substrate bonded joints under thermo-mechanical loading.

Starting with the available literature on the topic, the present work examined the effect of the thermo-mechanical and geometrical properties of the adhesives on the mechanical response of chemically bonded FRP-to-concrete joints both in a local and global sense. The problem is tackled numerically based on a mixed-mode interfacial cohesive law within a generalized node-to-segment (NTS) contact algorithm, which accounts for the effect of temperature-induced variations in material properties. The generalized NTS contact algorithm is capable of handling both separation and/or penetration conditions of the adhesive layer between the substrate and reinforcement, in a unified setting. The adhesive portion is modeled here by means of a bilinear traction-separation law, accounting for the interfacial damage evolution for different thermal conditions. A large numerical investigation is performed to check for the effect of the adhesive length and temperature-dependent mechanical properties on the overall bond behavior and debonding failure processes of the jointed specimens, whose results are successfully verified against the experimental predictions from literature.

The work is organized as follows. After this introduction, the theoretical framework of the problem is briefly reviewed in Section 2, both from a thermal and mechanical perspective. The numerical implementation is described in Section 3, where the numerical predictions are compared with a set of experimental data from the literature. The concluding remarks are reported in Section 4, whose general concepts could be extended to nonlinear adhesives or more complicated thermomechanical problems.

2 Theoretical framework

2.1 Definition of the thermomechanical properties

Polymers and their composites can be used under a varying range of thermal conditions (compared to the glass transition temperature T_g), such that it becomes important to evaluate their performances under temperature variations that may produce changes in physical–mechanical properties. It is well known that the mechanical properties of polymers depend on their molecular weight and temperature. Among them, the elastic normal and shear moduli $E(t, T)$ and $G(t, T)$ depend on time t and temperature T, where the polymer stiffness can vary due to possible molecular rearrangements. In Figure 1, for example, we plot the modulus *vs* temperature curve referred to a typical polymer with a secondary relaxation and a clear subdivision in four regions. It is worth noticing the glassy zone, where the elastic modulus can present two secondary transitions (named relaxation γ and β, respectively), and a third one, called glassy transition (or transition α). For higher temperatures, the glassy transition takes place in a transition zone with a decreasing value of the elastic modulus. Here, T_g is identified experimentally as the modulus inflecting point considering the temperature. Graphically, it can be obtained as the intersection between the tangents starting from the extreme points of the drastic modulus loss range. For higher temperatures, the rubbery zone is reached. Here the modulus has lower values and keeps constant, as visible in the third zone in Figure 1, with a plateau representing the elastic zone of the rubbery state. A mixed zone takes place, which features a rapid decrease in the elastic modulus. The polymer chain movement is described with the reptation concept, as introduced by De Gennes [78] for the first time in terms of wormlike movements of the chains. In the final viscous flow, the linear polymer becomes a viscous fluid with an abrupt reduction of the stiffness property. This is not true for crosslinked polymers due to their strong chemical bonds, so their modulus keeps almost constant until degradation is reached.

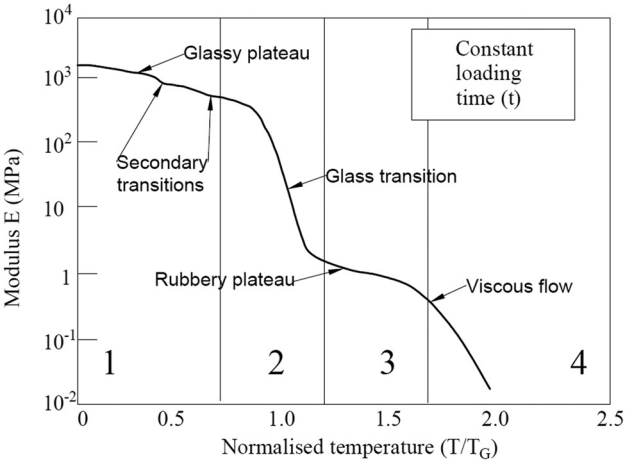

Figure 1: Elastic modulus of a linear polymer subjected to a temperature variation.

In order to employ polymer matrix composites in a transition zone, it is necessary to describe analytically the polymer property variation (*e.g.*, the stiffness) caused by a temperature change. Mahieux [79,80] studied this problem and proposed a relation valid for every type of polymer (thermosetting, thermoplastic, amorphous, linear, semicrystalline, and crosslinked), for every molecular weight, and for a full range of temperature. In the rubbery zone, the temperature dependence of the stiffness property E can be defined as follows:

$$E = \frac{\rho \mathrm{RT}}{M_C}, \tag{1}$$

where ρ is the density, RT is the room temperature, and M_C is the molecular weight. However, this is true only for temperatures higher than the glass transition temperature T_g.

Different theories allow us to define the variation of the elastic properties in the glassy state but only for small variations. Among many, the van Krevelen [81] theory suggests the following relations:

$$\frac{G_g(T)}{G_g(T_r)} = \frac{T_g/T_r + 2}{T_g/T_r + 2T/T_r} \text{ for } T < T_g, \tag{2}$$

$$\frac{G_C(T)}{G_C(T_r)} = \exp\left[-2.65\frac{T_m/T_r - T_m/T}{T_m/T_r - 1}\right] \text{ for } T > T_r - 100, \tag{3}$$

$$G_{SC} = G_g + x_C^2(G_C - G_g), \tag{4}$$

where G is the shear modulus; T is the temperature; and the subscripts g, c, sc, m, and r refer to the glassy,

crystalline, semi-crystalline, melting, and reference states, respectively. Also, in this case, note that these equations can be applied only to the glassy state (service temperature lower than T_g), and do not refer to the polymer microstructure.

Among different possibilities, in this study, Mahieux's approach [80] is adopted due to its general nature with respect to other existing theories. Such approach, indeed, describes the polymer behavior on a full-range temperature, including the transitions, and relates the polymer mechanical response to its microstructure. For a consistent definition of the local behavior for such material, during its relaxation time, spring and dashpots (dampers that withstand displacement through viscous friction) are considered in the model, such that the Young's modulus $E(t)$ varies with time t as follows:

$$E(t) = \sum_{i=1}^{N} E_i e^{-t/\tau_i}, \tag{5}$$

where τ_i is the relaxation time. Such equation can be written in an integral form as

$$E(t) = \int_{-\infty}^{+\infty} H(\tau) e^{-t/\tau} \mathrm{d}(\ln \tau), \tag{6}$$

where H is a distribution function, defined as

$$H(\tau) = \tau E(\tau). \tag{7}$$

In the viscous region, the polymer reptation is usually modeled as follows:

$$E \propto e^{-Q/(\mathrm{RT})}, \tag{8}$$

with Q being the activation energy of the process. The Boltzmann distribution denotes a casual process, so that the bonds are broken following an indeterminate sequence, while the Weibull distribution allows us to describe an interactive fracturing process. Note that bond breaking influences the other bonds: for example, the secondary transitions (Figure 1) result from highly localized molecular movements. Therefore, the secondary bonds must be broken to allow movement of a lateral group or a few principal chains. Due to the atomic distance variation, which induces an interaction force distribution, the secondary bonds break in different moments. Compared to the Boltzmann distribution, the Weibull distribution seems to provide a more reliable mathematical representation of the debonding process and accounts for the secondary transition β. The mechanical response is given by the movement of little chain segments (monomers). Given the high number and force of the bonds involved in this relaxation process, it is possible to associate a Weibull coefficient m_1 with transition β, so that Eq. (5) becomes

$$H_1(\tau) = e^{-(t/\tau_1)^{m_1}}. \tag{9}$$

By substitution of time τ_1 with the characteristic instantaneous temperature and by introducing a conversion constant, we have

$$H_1(T) = H_1^0 e^{-(T/\beta_1)^{m_1}}, \tag{10}$$

where β_1 is a characteristic temperature (the transition temperature beta) and H_1^0 beta transition (*i.e.*, the relaxation entity). The same approach can be applied to the other transitions for an improved number of segments involved in the relaxation stage. A novel Weibull coefficient can be associated with each stage, which refers to the number of intermolecular bonds involved. For this reason, a more general law can be applied to all transformation stages by adding all their components

$$E = \sum_{i=1}^{N} H_i e^{-(T_i/T_{\mathrm{ref},i})^{m_i}}. \tag{11}$$

Commercial polymers typically feature from one up to three transitions ($1 \le N \le 3$), whose coefficients H_i (magnitude of phase transition) can be defined with different methods. Hereafter, we assume the following thermal dependence of the elastic modulus [79], as plotted in Figure 2.

- For materials that are not subjected to any transition before becoming rubbery/viscous

$$E = E_3 e^{-(T/T_3)^{m_3}}. \tag{12}$$

- For materials featuring two transitions

$$E = (E_2 - E_3) e^{-(T/T_2)^{m_2}} + E_3 e^{-(T/T_3)^{m_3}}. \tag{13}$$

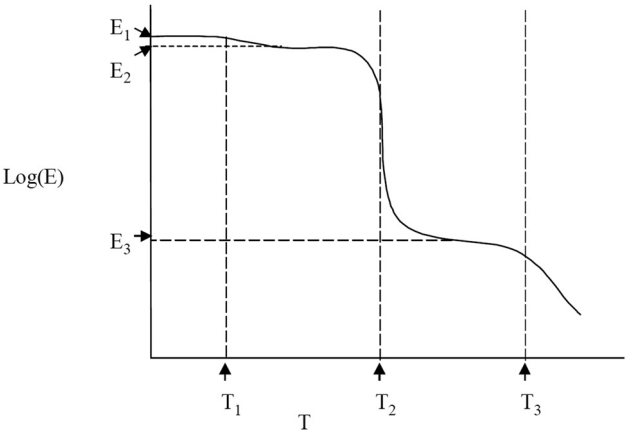

Figure 2: Definition of the input parameters for the $E-T$ relation.

– For materials featuring three transitions

$$E = (E_1 - E_2)e^{-(T/T_1)^{m_1}} + (E_2 - E_3)e^{-(T/T_2)^{m_2}} + E_3 e^{-(T/T_3)^{m_3}}. \quad (14)$$

In these three relations, temperatures (T_i) are expressed in Kelvin (K) and refer to each transition phase depicted in Figure 2. The thermal values can be defined considering the maximum points of the curve resulting from a dynamic mechanic analysis or considering the inflection points of a differential scanning calorimetry curve. At the same time, E_i corresponds to the instantaneous stiffness modulus assumed by the material at the beginning of a transition phase: E_1 is the instantaneous modulus of the polymer for low temperatures, E_2 is the instantaneous modulus immediately after the beta transition, and E_3 is the instantaneous modulus at the beginning of the rubbery state (Figure 2). Moreover, the parameters m_i stand for the Weibull coefficients related to the stress distribution during a debonding phenomenon. The value of m is small if there is a wide distribution of the bonding forces, and it becomes high for homogeneous materials with a limited distribution of bonding forces, or amorphous materials. Moreover, the m value depends on the impediment degree of a molecular motion (*i.e.*, crosslinking, molecular weight, crystallinity): if the motion is limited, m assumes a low value; if the motion is strictly limited, m becomes much lower, getting a similar behavior to the Boltzmann distribution. In the viscous flow and for cross-links, the gradient slope decreases for an increased cross-linking degree. For highly cross-linked materials, the viscous flow can disappear.

2.2 Interfacial constitutive law and finite-element algorithm

For a numerical description of the mixed mode debonding process, an uncoupled cohesive law is here assumed to model the adhesive interface within the FRP-to-concrete joint both in the normal and tangential directions. An uncoupled cohesive zone model is here selected, as typically used when the interface separation is enforced to occur in a single predefined direction, such that either Mode I and II separations occur. This means that the normal and tangential stresses, p_N and p_T, depend on the relatively normal and tangential displacement, g_N, and g_T, separately.

This choice derives from the possibility of using different values of interfacial fracture energies for both Mode I and Mode II, in line with the experimental evidence. For a compressive state in the normal direction (*i.e.*, for $g_N < 0$ and $p_N < 0$), we enforce a non-penetration condition by using a Penalty method, within a generalized contact algorithm, based on the minimization of a modified potential $\bar{W} = W + W_C$, which involves both the elastic part W and contact part, $W_C = \varepsilon_N g_N$, with ε_N being the Penalty parameter. We select a bilinear cohesive traction-separation law for the normal and shear directions (Figure 3) because of its capability to simply define the main three interfacial properties, namely, the fracture energies, the cohesive strengths $p_{N\,max}$ and $p_{T\,max}$, and the elastic stiffness [82]. For such simple reasons, the bilinear model is largely used, also in design guidelines, to model the FRP-to-brittle substrate interfaces [83] in lieu of more complicated nonlinear models. Thus, the energy release rates for

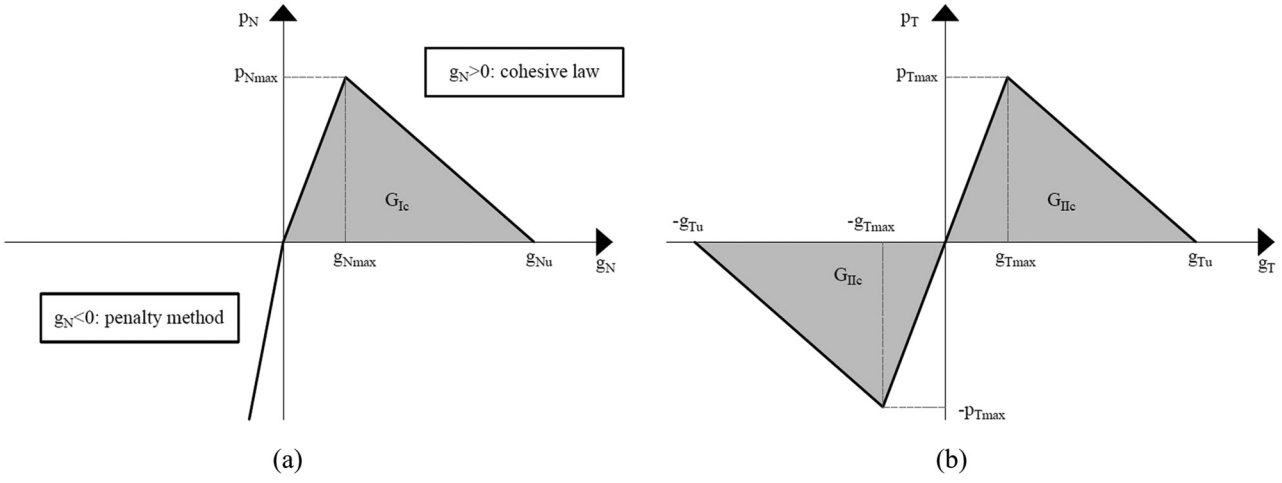

Figure 3: Relation at the interface between the traction and the relative displacement: (a) normal direction and (b) tangential direction.

Modes I and II correspond to the areas under the respective curves, integrated up to the current values of g_N and g_T [84], such that a mixed mode fracture criterion must be properly introduced to govern a failure process. In the present work, we selected one of the simplest possible criteria to handle the fracturing process, *i.e.*,

$$\frac{G_I}{G_{Ic}} + \frac{G_{II}}{G_{IIc}} = 1, \tag{15}$$

where G_{IC} and G_{IIC} stand for the fracture energies in pure Modes I and II, respectively.

A generalized NTS contact element is adopted to handle the interfacial problem for both the normal and tangential forces within a unified formulation, as also described in the study of Dimitri *et al.* [24]. Based on the contact status, an automatic switching procedure is applied to select a cohesive or contact model. Each element contribution, for both cohesive and contact forces, is automatically added to the virtual global work as

$$\delta W_C = F_N \delta g_N + F_T \delta g_T, \tag{16}$$

where $F_N = p_N A$ and $F_T = p_T A$ stand for the normal and tangential interfacial forces, and A is the contact area associated with each contact element.

Figure 4 depicts the geometrical scheme of the selected FRP-to-concrete pull-out test. From a numerical standpoint, the adherend is discretized with 2D linearly elastic beam elements, while the concrete substrate is modeled with plane-stress four-node isoparametric elastic elements.

The nonlinear problem is solved with a Newton–Raphson iterative scheme, where the global tangent stiffness matrix is consistently obtained from a linearization of all the terms in Eq. (16). Such linearization yields the following relation:

$$\begin{aligned}\Delta\delta W_C = &\left(\frac{\partial F_N}{\partial g_N}\Delta g_N + \frac{\partial F_N}{\partial g_T}\Delta g_T\right)\delta g_N \\ &+ \left(\frac{\partial F_T}{\partial g_T}\Delta g_N + \frac{\partial F_T}{\partial g_T}\Delta g_T\right)\delta g_T + F_N \Delta\delta g_N + F_T \Delta\delta g_T,\end{aligned} \tag{17}$$

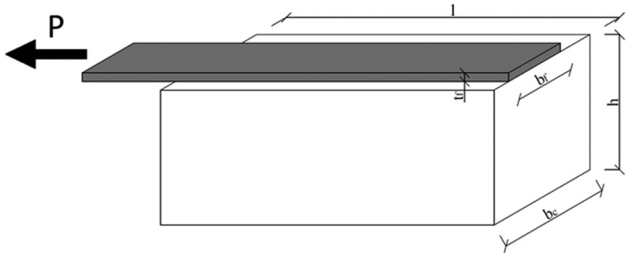

Figure 4: Setup of the single-lap shear test.

where δ and Δ refer to the virtual variation and linearization, respectively. For more details about the geometrical quantities δg_N, δg_T, Δg_N, Δg_T, $\Delta\delta g_N$, and $\Delta\delta g_T$, the reader is referred to Ref. [85]. The partial derivatives of the normal and shear forces with respect to the normal and shear relative displacements depend on the cohesive law parameters. According to the selected traction separation law (Figure 3), it is

$$\frac{\partial F_N}{\partial g_N} = \begin{cases} \varepsilon_N A & \text{for} \quad g_N < 0, \\ \dfrac{p_{N\,max}}{g_{N\,max}} A & \text{for} \quad 0 \le g_N < g_{N\,max}, \\ -\dfrac{p_{N\,max}}{g_{Nu} - g_{N\,max}} A & \text{for} \quad g_{N\,max} \le g_N < g_{Nu}, \end{cases} \tag{18}$$

$$\frac{\partial F_T}{\partial g_T} = \begin{cases} \dfrac{p_{T\,max}}{g_{T\,max}} A & \text{for} \quad |g_T| < g_{T\,max}, \\ -\dfrac{p_{T\,max}}{g_{Tu} - g_{T\,max}} A & \text{for} \quad g_{T\,max} \le |g_T| < g_{Tu}, \end{cases} \tag{19}$$

$$\frac{\partial F_N}{\partial g_T} = \frac{\partial F_T}{\partial g_N} = 0. \tag{20}$$

3 Numerical analysis

A large numerical investigation is now performed for the pull-out test set-up illustrated in Figure 4, whose mechanical properties are here selected in line with the experimental tests performed in the study of Takeo *et al.* [86], for comparative purposes. A parametric study aims at analyzing the sensitivity of the mechanical response to different geometrical and mechanical properties of the FRP reinforcement and adhesive phases, accounting for different possible thermal conditions. The analysis starts considering the geometrical parameters in Table 1, where l, h, and b_c stand for the length, height, and width of the concrete substrate, respectively, and t_f and b_f stand for the reinforcement thickness and width, respectively. The initial specimen accounts for a concrete substrate with elastic modulus $E_c = 32.8$ GPa and reinforced with an FRP sheet with elastic modulus $E_f = 230$ GPa, which is tested, in displacement-control mode, up to a total displacement $d = 0.35$ mm (Table 1). As far as the adhesive layer is concerned, the main interfacial parameters are taken as summarized in Table 2. More specifically, we assume an elastic stiffness $k_N = 2{,}600$ MPa and $k_T = 1{,}100$ MPa in the normal and shear direction, respectively, a Penalty parameter in compression $\varepsilon_N = 3{,}000$ MPa, ultimate values of the normal and shear relative displacements $g_{Nu} = 0.2$ mm and $g_{Tu} = 0.4$ mm, and cohesive strengths $p_{N\,max} = 40$ MPa and $p_{T\,max} = 120$ MPa, in line with the experimental

Table 1: Geometric and mechanical data

l [mm]	h [mm]	b_c [mm]	t_f [mm]	b_f [mm]	E_c [MPa]	E_f [MPa]	d [mm]
150	150	150	0.167	100	32,800	2,30,000	0.35

Table 2: Adhesive data implemented in the code

k_N [MPa]	k_T [MPa]	$p_{N\,max}$ [MPa]	$p_{T\,max}$ [MPa]	g_{Nu} [mm]	g_{Tu} [mm]	ε_N [MPa]
2,600	1,100	40	120	0.2	0.4	3,000

findings by Takeo *et al.* [86]. Hereafter, the same example is repeated systematically to study the effect of the bond length l, the elastic modulus of the reinforcing phase, E_f, and the reinforcement thickness and length, t_f, b_f, respectively, on the overall response of the specimen in terms of load–displacement curves and peak load.

3.1 Effect of bond length

The numerical test is repeated for an increased value of the bond length l from 50 up to 400 mm in steps of 50 mm, keeping the other parameters constant, as summarized in Table 3 and Figure 5, together with the corresponding peak load P_{max}. It is worth observing that an increased bond length of the FRP on the substrate up to 200 mm yields larger peak loads, beyond which it remains almost constant, in line with findings by Takeo *et al.* [86] and Ueda *et al.* [87]. Similar comments can be repeated by looking at the force–displacement curves in Figure 6, which clearly show an increased initial stiffness (in the ascending branch together with an increased value of the peak load and an increased displacement capacity of the specimen, because of an improved transfer of local interfacial stresses among FRP and substrate in the bonded portion, especially in the shear direction. It is expected, indeed, that an increased bond length increases the Mode II stress components, in lieu of decreased values of Mode I stresses, and an overall decrease of the interfacial mixed-mode stress distribution within the specimen.

Table 3: Variation of the maximum load for different bond lengths

l [mm]	P_{max} [N]	l [mm]	P_{max} [N]
50	5,723.2	250	13,488
100	10,106	300	13,533
150	12,466	350	13,548
200	13,287	400	13,555

3.2 Effect of the reinforcement elastic modulus

The analysis has been extended by considering three different types of composite reinforcement, namely, a glass

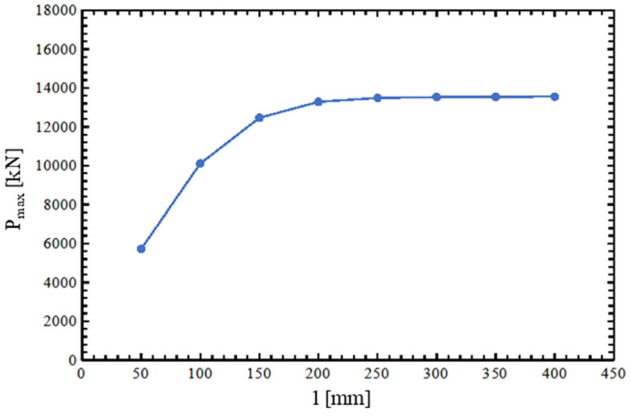

Figure 5: Variation of the maximum load with the bond length.

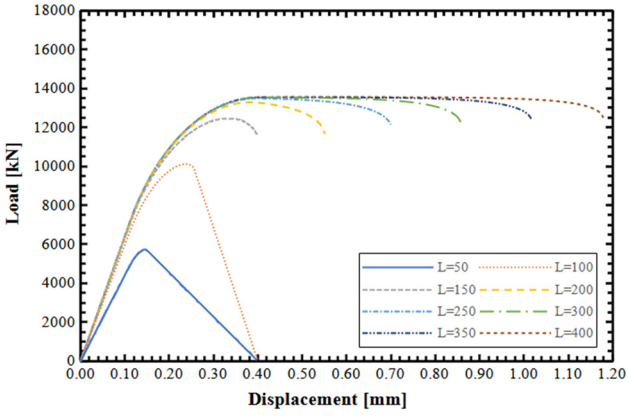

Figure 6: Load–displacement curves for different bond lengths.

Table 4: Variation of the maximum load for different reinforcement elastic moduli

E_f [GPa]	P_{max} [N]	E_f [GPa]	P_{max} [N]
100	8,863.9	230	12,466
150	10,625	250	12,799
190	11,663	390	14,362
210	12,090	450	14,775

FRP with an elastic modulus E_f = 100 GPa (labeled as GFRP100), an aramid FRP with E_f = 150 GPa (labeled as AFRP150), and a carbon-based reinforcement (CFRP) with a different elastic modulus E_f of 190, 210, 230, 250, 390 and 450 GPa, while keeping all the other parameters constant.

In Table 4 and Figure 7, the variation of the maximum load for a varying elastic stiffness of the FRP strip is summarized. As also expected experimentally in the study of Wu *et al.* [88], the maximum load significantly increases for an increased elastic modulus E_f, reaching the highest values for a CFRP with E_f = 390 ÷ 450 GPa. In these last cases, however, the numerical values of P_{max} are more conservative than expected experimentally by Wu *et al.* [88], because of the adhesive crisis estimations in lieu of their cohesive experimental results found in [88]. This can be addressed to the local behavior of the concrete which may exhibit higher properties with respect to the theoretical prediction. The overall load–displacement response of the specimen is, thus, plotted in Figure 8 for different FRPs. Based on these plots, note that as the elastic modulus E_f of the FRP increases, the slope of the curves in the ascending branch increases, together with an increased peak strength P_{max} and interfacial brittleness in the descending branch of the curves.

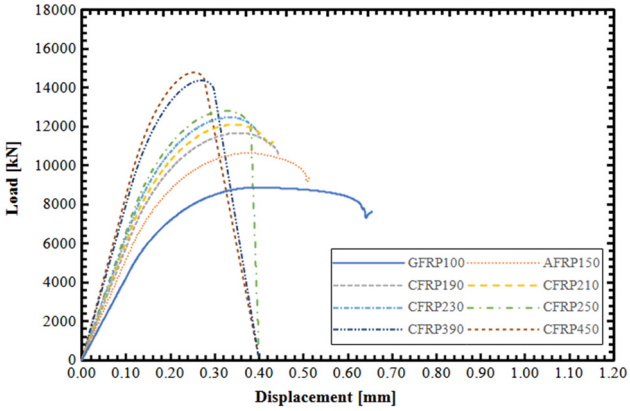

Figure 8: Load–displacement curves for different fiber elastic moduli.

3.3 Effect of the reinforcement thickness

We now assume six different FRP thicknesses t_f, *i.e.*, 0.167, 0.222, 0.247, 0.337, 0.55, and 1.4 mm, as commonly used in structural reinforcements. All the other parameters are kept constant. The results are plotted in Figures 9 and 10 and could be compared to the experimental predictions by Ueda *et al.* [87] and Tan [89]. Even in this case, an increased value of the fiber thickness corresponds to an increased value of the peak load of 7 ÷ 8.5%, see also the results in Table 5. As also plotted in Figure 10, the global load–displacement curves increase their initial slope in the ascending branch for an increased reinforcement thickness. At the same time, the maximum strength of the specimen tends to increase, and the specimen tends to assume an elastic-brittle behavior up to the final collapse, for an increased reinforcement thickness.

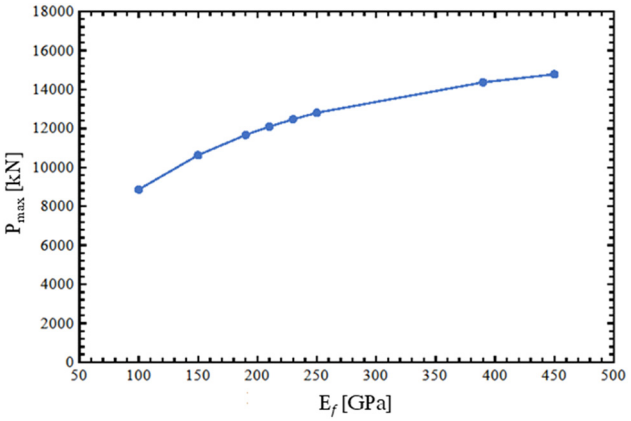

Figure 7: Variation of the maximum load with the elastic modulus of the reinforcement.

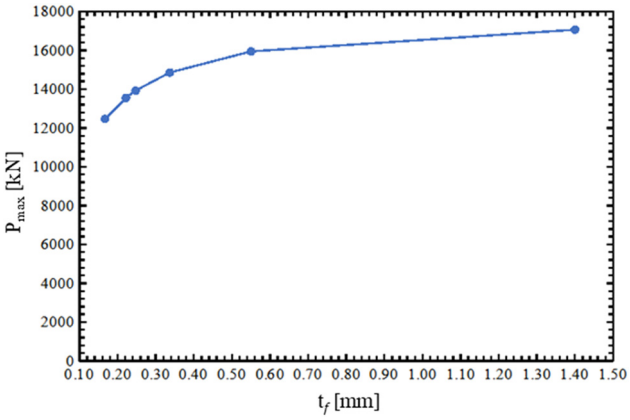

Figure 9: Variation of the maximum load with the fiber thickness.

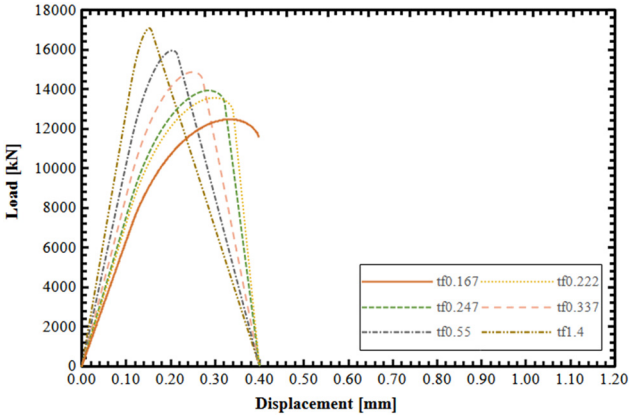

Figure 10: Load–displacement curves for different fiber thicknesses.

3.4 Effect of the FRP width

The reinforcement width represents another key parameter that can significantly affect the global mechanical behavior of the adhesive joint. A larger dimension of the reinforcing FRP, indeed, can improve the interfacial distribution of stresses, and the related maximum debonding load of the specimen, whose sensitivity is studied here, by selecting the following combinations:

1. b_c = 150 mm and b_f 50, 60, 80 and 100 mm;
2. b_c = 200 mm and b_f 120 and 150 mm; and
3. b_c = 400 mm and b_f 200 and 300 mm,

while keeping all the other parameters constant.

As summarized in Table 6 and plotted in Figure 11, the maximum load P_{max} increases monotonically for higher values of b_f, with increased structural stiffness and decreased ductility, as visible in the global load–displacement response in Figure 12. An increased interfacial stiffness, indeed, is expected to yield a more localized distribution of the cohesive stresses in the bond length, with an increased overall fragility of the specimen. Even in this case, the numerical insights are comparable with the experimental findings by Ueda *et al.* [87] and Tan [89].

3.5 Effect of temperature

We now analyze the possible effect of temperature on the mechanical bond properties of concrete members externally strengthened with FRPs while selecting an epoxy adhesive with a glass transition temperature T_g ranging between 50 and 80°C. Epoxy adhesives are noteworthy for their susceptibility to mechanical degradation when exposed to high temperatures. Since adhesives are responsible for the bonding behavior among FRPs and concrete, for bond-critical conditions, the structural efficiency of the strengthening system could be highly influenced during a high-temperature exposure [90]. Based on the experimental observations from literature on shear tests, when the temperature in the FRP exceeds 200°C, the reinforcement does not contribute anymore to the load-bearing capacity, because of a softening bonding adhesion, with a general loss of the adhesive transfer between materials and a premature detachment of the FRP from the adherend. Due to the low glass transition temperature of adhesives, their elastic modulus decays drastically at temperatures slightly higher than the ambient ones. In such a context, it is important to define a theoretical correlation between temperature and the global response of the reinforced specimen. Two adhesives are considered, labeled as "Adhesive 1" and "Adhesive 2," with elastic moduli of 4,157 MPa and 2,595 MPa, respectively. Both adhesives feature two different transition phases, moving from the glassy zone to the rubbery state, such that they lose any reserve of resistance for temperatures higher than 150–200°C. In what

Table 5: Variation of the maximum load with the fiber thickness

t_f [mm]	P_{max} [N]	t_f [mm]	P_{max} [N]
0.167	12,466	0.337	14,858
0.222	13,553	0.55	14,944
0.247	13,926	1.4	17,066

Table 6: Variation of the maximum load with the fiber lengths

b_f [mm]	P_{max} [N]	b_f [mm]	P_{max} [N]
50	9,457.5	120	13,180
60	10,256	150	14,018
80	11,525	200	14,897
100	12,466	300	15,843

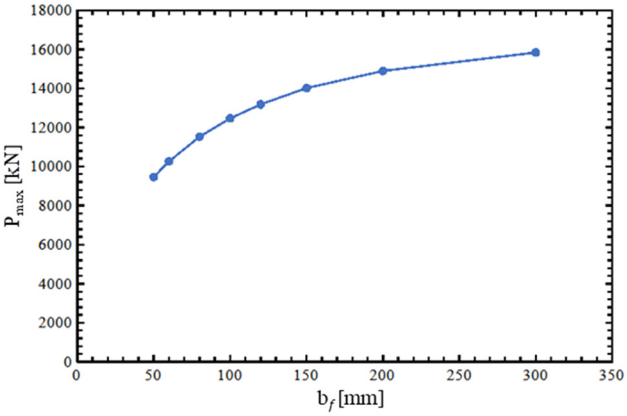

Figure 11: Variation of the maximum load with the reinforcement width.

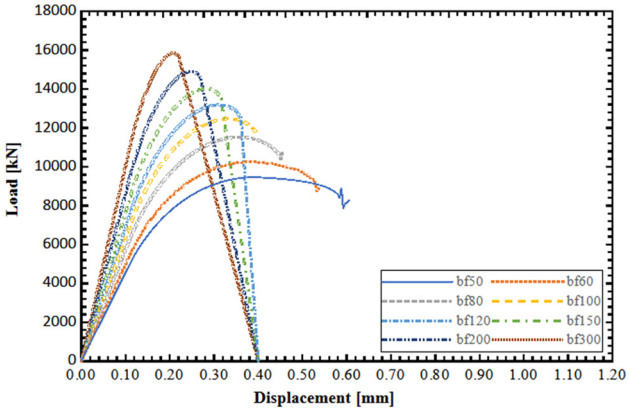

Figure 12: Load–displacement curves for different reinforcement widths.

follows, we refer to the relation proposed by Mahieux [79] to define the variation of the elastic stiffness E, with temperature T

Table 7: Input parameters

	E_2 [MPa]	E_3 [MPa]	T_2 [°C]	T_3 [°C]	m_2	m_3
Adhesive 1	4,156	300	64	120	60	40
Adhesive 2	2,595	150	128	183	20	20

$$E = (E_2 - E_3)e^{-(T/T_2)^{m_2}} + E_3 e^{-(T/T_3)^{m_3}}, \tag{21}$$

where T_i refers to temperatures at each transition, E_i is the instantaneous stiffness of the adhesive at the beginning of each plateau region, and m_i are the Weibull coefficients, which account for the microstructure of a polymer and the statistics of the bond breakage. More specifically, E_2 and E_3 stand for the instantaneous moduli right after the beta transition and at the beginning of the rubbery plateau, which occur at temperatures T_2 and T_3, respectively. Based on the experimental data in previous studies [80,91,92], we set high values of m_i for amorphous

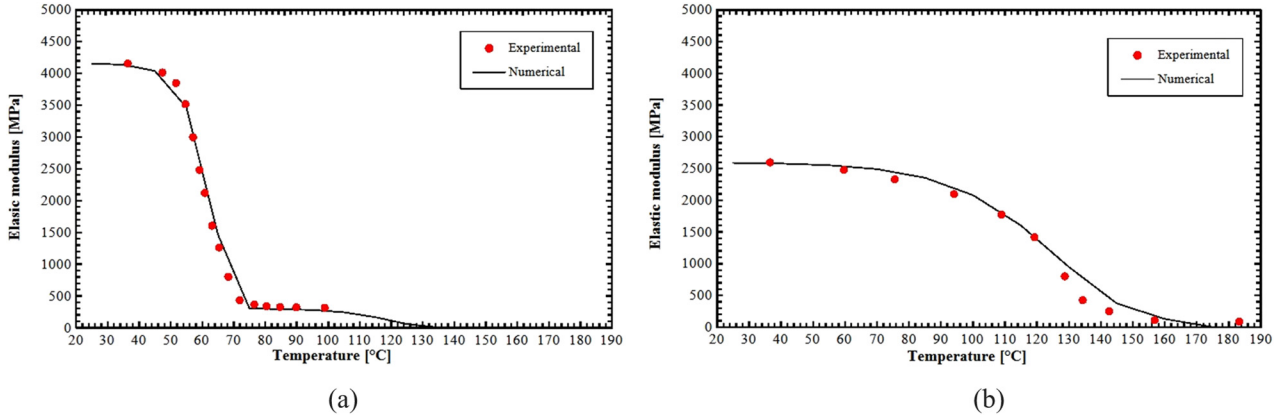

Figure 13: Variation of the elastic modulus of resins with temperature: (a) Adhesive 1 and (b) Adhesive 2.

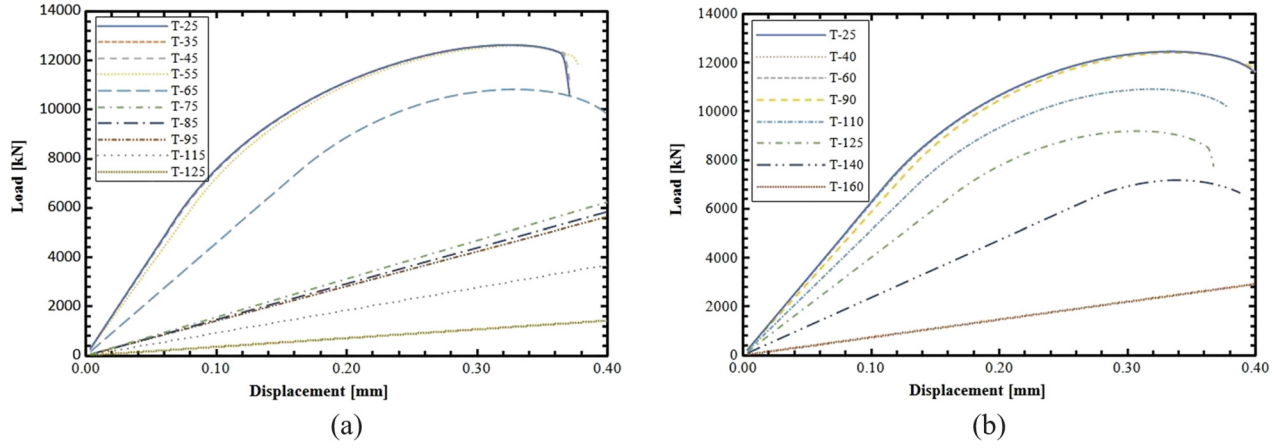

Figure 14: Load–displacement response for different temperatures: (a) Adhesive 1 and (b) Adhesive 2.

Table 8: Variation of the elastic properties of the adhesives with the temperature

T [°C]	E [MPa]	G [MPa]
Adhesive 1		
25	4,154	1,731
35	4,139	1,724
45	4,039	1,683
55	3,466	1,444
65	1,467	611
75	302	126
85	293	122
95	279	116
115	165	69
125	57	24
Adhesive 2		
25	2,589	1,079
40	2,578	1,074
60	2,536	1,057
90	2,281	950
110	1,786	744
125	1,174	489
140	534	222
160	129	54

Table 9: Variation of the maximum load with temperature

T [°C]	P_{max} [N]
Adhesive 1	
25	12,634
35	12,633
45	12,624
55	12,575
65	10,825
75	7,251.4
85	6,588.4
95	6,588.6
115	4,738.2
125	2,823.1
Adhesive 2	
25	12,458
40	12,456
60	12,449
90	12,404
110	10,912
125	9,190.7
140	7,173.5
160	4,011.5

adhesives with homogeneous properties (see Adhesive 1) and narrow distribution of bond strengths, while setting lower values of m_i for crosslinked adhesives with a reduced slope of the drop in the viscous flow region (see Adhesive 2). All the selected parameters for Eq. (21) are reported in

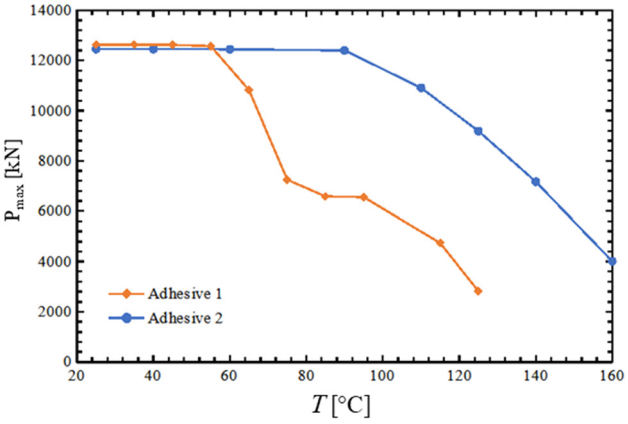

Figure 15: Variation of the maximum load with temperature.

Table 7, whereas Figures 13 and 14 show the theoretical and experimental variation of the stiffness with temperature, with a good matching among results. Based on a comparative evaluation of the plots in Figure 13a and b, it is worth observing the different behavior in the glass transition zone, with a rapid modulus drop for "Adhesive 1" in lieu of a gradual reduction with temperature for "Adhesive 2," thus leading to a different behavior of the two adhesives in the rubbery state. Starting with the theoretical variation of the stiffness properties in Eq. (21) for the adhesive layer, we now analyze the sensitivity of the debonding response for the selected pull-out tests, both in terms of maximum load and global time histories. The systematic investigation accounts for the normal and shear elastic stiffness at different temperatures as summarized in Table 8 for both adhesives, whose properties are responsible for the slopes in the ascending branch of the interfacial model in Modes I and II. The numerical tests are performed in displacement control mode.

Figure 14 shows the load–displacement curves for Adhesive 1 (Figure 14a), and Adhesive 2 (Figure 14b), with a noteworthy variation of the global response for an increased temperature, both in the ascending and softening branches. An increased temperature, indeed, drastically reduces the elastic stiffness and the maximum load of all the specimens, while extending the elastic stage for all the specimens, especially for temperatures higher than T_g, when adhesives reach the rubbery state, due to an increased molecular motion and overall deformability. At the same time, we summarize the variation of P_{max} with temperature in Table 9, whose results are also plotted in Figure 15 for both adhesives, with a maximum reduction of about 78% for $T = 125°$ and $T = 160°$ for Adhesives 1 and 2, respectively. Note that P_{max} remains almost constant for $T < T_g$ and decreases monotonically when the

glass transition takes place, as also expected from experimental evidences. Specimens based on the second adhesive feature a more gradual decay of $P_{\max}$ compared to the first adhesive, thus reflecting in a global sense, the local decay of the interfacial properties. Moreover, for "Adhesive 2", $P_{\max}$ starts decreasing for a higher temperature compared to that one based on "Adhesive 1." For affinity reasons among the global response of $P_{\max}$ *vs* T plotted in Figure 15 and the local properties of adhesives in Figure 13, we propose the following relation among the debonding load $P_{\max}$ and temperature T, which could serve as a useful theoretical tool for design purposes, namely

$$P_{\max}(T) = \sum_{i=1}^{N} \alpha F_i e^{-(T_i/T_{\mathrm{ref},i})^{\beta_i}}, \tag{22}$$

where α_i and β_i are parameters that depend on the transition states to which the adhesive is subjected, F_i is a force parameter for a specific transition state occurring at temperature T_i, and $T_{\mathrm{ref},i}$ is a reference temperature. This formulation can be considered as a starting point for future theoretical and experimental developments on the topic, in order to assess and improve the durability of glued joints, and to improve the load-bearing capacities of strengthened structural elements.

4 Conclusions

A novel research has been carried out on the numerical modeling of the FRP-concrete bond behavior in single shear tests, subjected to a thermal variation. The problem has been approached computationally based on a contact NTS algorithm capable of handling a mixed-mode failure within a unified formulation, accounting for the effect of thermal variations on the interfacial properties of adhesives. A bilinear traction-separation law is proposed here to model the adhesive layer, which accounts for the interfacial damage evolution, under different thermal conditions. A large numerical investigation was performed to check for the effect of the adhesive geometrical properties and temperature-dependent mechanical properties on the overall bond behavior and failure modes of the selected specimens. The numerical results have been successfully verified against the experimental predictions available from the literature. Despite the simplicity of the proposed algorithm, it appears capable of capturing different aspects of the physical behavior, namely, the variation of the stiffness, displacement capacity, and maximum load for a varying bond length, FRP thickness, width, and mechanical properties of the materials. The pioneering research by Mahieux and Reifsnider [80] has been considered for the theoretical relationship between the elastic modulus of polymers and temperature within the NTS formulation in order to check for the sensitivity of the global response in terms of time history and maximum capacity for temperature-dependent adhesive properties. Based on the results, a temperature increase over the transition level, decreases the maximum load and stiffness, due to a local variation of primary and secondary bonds within polymer adhesives at a microscale, together with a varied molecular motion and decay of their elastic stiffness. A theoretical model has been, also, proposed as a useful design tool to relate the debonding load of jointed specimens and temperature, which consistently reflects, at a macroscale level, the physical and mechanical properties of adhesive resins at the microscale.

Funding information: The authors state no funding involved.

Author contributions: All authors have accepted responsibility for the entire content of this manuscript and approved its submission.

Conflict of interest: Rossana Dimitri and Francesco Tornabene, who are the co-authors of this article, are current Editorial Board members of *Curved and Layered Structures*. This fact did not affect the peer-review process. The authors declare no other conflict of interest.

References

[1] Pepe M, Mazaheripour H, Barros J, Sena-Cruz J, Martinelli E. Numerical calibration of bond law for GFRP bars embedded in steel fibre-reinforced self-compacting concrete. Compos B Eng. 2013;50:403–12.
[2] Ghiassi B, Marcari G, Oliveira DV, Lourenço PB. Numerical analysis of bond behavior between masonry bricks and composite materials. Eng Struct. 2012;43:210–20.
[3] Teng JG, Chen JF, Smith ST, Lam L. FRP: Strengthened RC structures. West Sussex, UK: John Wiley and Sons Ltd; 2002. p. 31–46.
[4] Barros J, Dias SJ, Lima JL. Efficacy of CFRP-based techniques for the flexural and shear strengthening of concrete beams. Cem Concr Compos. 2007;29(3):203–17.
[5] Hollaway LC, Teng JG. Strengthening and rehabilitation of civil infrastructures using fiber-reinforced polymer (FRP) composites. Sawston, UK: Woodhead Publishing Ltd.; 2008.
[6] Teng JG, Yu T, Fernando D. Strengthening of steel structures with fiber-reinforced polymer composites. J Constr Steel Res. 2012;78:131–43.

[7] Teng JG, Smith ST, Yao J, Chen JF. Intermediate crack-induced debonding in RC beams and slabs. Constr Build Mater. 2003;17(6–7):447–62.
[8] Teng JG, Chen JF. Mechanics of debonding in FRP-plated RC beams. Proc Inst Civ Eng: Struct Build. 2009;162(5):335–45.
[9] Realfonzo R, Martinelli E, Napoli A, Nunziata B. Experimental investigation of the mechanical connection between FRP laminates and concrete. Compos B Eng. 2013;45(1):341–55.
[10] Täljsten B. Strengthening of concrete prisms using the plate-bonding technique. Int J Fract. 1996;82(3):253–66.
[11] Chen JF, Teng JG. Anchorage strength models for FRP and steel plates bonded to concrete. J Struct Eng. 2001;127(7):784–91.
[12] Dai JG, Ueda T. Local bond stress slip relations for FRP sheets-concrete interfaces. In: Tan KH, editor. Fibre Reinforced Polymer Reinforcement for Concrete Structures (In 2 Volumes): Proceedings of the Sixth International Symposium on FRP Reinforcement for Concrete Structures (FRPRCS-6); 2003 Jul 2–10; Singapore. World Scientific, 2003. p. 143–52.
[13] Dai J, Ueda T, Sato Y. Development of the nonlinear bond stress–slip model of fiber reinforced plastics sheet–concrete interfaces with a simple method. J Compos Constr. 2005;9(1):52–62.
[14] Lu XZ, Teng JG, Ye LP, Jiang JJ. Bond–slip models for FRP sheets/plates bonded to concrete. Eng Struct. 2005;27(6):920–37.
[15] Lu XZ, Ye LP, Teng JG, Jiang JJ. Meso-scale finite element model for FRP sheets/plates bonded to concrete. Eng Struct. 2005;27(4):564–75.
[16] Fawzia S, Al-Mahaidi R, Zhao XL. Experimental and finite element analysis of a double strap joint between steel plates and normal modulus CFRP. Compos Struct. 2006;75(1–4):156–62.
[17] Leung CK, Yang Y. Energy-based modeling approach for debonding of FRP plate from concrete substrate. J Eng Mech. 2006;132(6):583–93.
[18] Seracino R, Raizal Saifulnaz MR, Oehlers DJ. Generic debonding resistance of EB and NSM plate-to-concrete joints. J Compos Constr. 2007;11(1):62–70.
[19] Bocciarelli M, Colombi P, Fava G, Poggi C. Prediction of debonding strength of tensile steel/CFRP joints using fracture mechanics and stress based criteria. Eng Fract Mech. 2009;76(2):299–313.
[20] Baky HA, Ebead UA, Neale KW. Nonlinear micromechanics-based bond–slip model for FRP/concrete interfaces. Eng Struct. 2012;39:11–23.
[21] Kashyap J, Willis CR, Griffith MC, Ingham JM, Masia MJ. Debonding resistance of FRP-to-clay brick masonry joints. Eng Struct. 2012;41:186–98.
[22] Biolzi L, Ghittoni C, Fedele R, Rosati G. Experimental and theoretical issues in FRP-concrete bonding. Constr Build Mater. 2013;41:182–90.
[23] Dai JG, Gao WY, Teng JG. Bond-slip model for FRP laminates externally bonded to concrete at elevated temperature. J Compos Const. 2013;17(2):217–28.
[24] Dimitri R, Trullo M, De Lorenzis L, Zavarise G. Coupled cohesive zone models for mixed-mode fracture: A comparative study. Eng Fract Mech. 2015;148:145–79.
[25] Chajes MJ, Finch WW, Thomson TA. Bond and force transfer of composite-material plates bonded to concrete. Struct J. 1996;93(2):209–17.
[26] Maeda T. A study on bond mechanism of carbon fiber sheet. Proceeding of the Third International Symposium of Non-metallic (FRP) Reinforced for Concrete Structures. Vol. 1. Sapporo, Japan: Japan Concrete Institute; 1997. p. 279–86.
[27] Brosens K, Van Gemert D. Anchorage design for externally bonded carbon fiber reinforced polymer laminates. Spec Publ. 1999;188:635–46.
[28] Bizindavyi L, Neale KW. Transfer lengths and bond strengths for composites bonded to concrete. J Compos Constr. 1999;3(4):153–60.
[29] Focacci F, Nanni A, Bakis CE. Local bond-slip relationship for FRP reinforcement in concrete. J Compos Constr. 2000;4(1):24–31.
[30] Brosens K. Anchoring of externally bonded steel plates and CFRP laminates for the strengthening of concrete elements [dissertation]. Leuven: Katholieke Universiteit Leuven; 2001.
[31] Nakaba K, Kanakubo T, Furuta T, Yoshizawa H. Bond behavior between fiber-reinforced polymer laminates and concrete. Struct J. 2001;98(3):359–67.
[32] Yao J, Teng JG, Chen JF. Experimental study on FRP-to-concrete bonded joints. Compos B Eng. 2005;36(2):99–113.
[33] Dai J, Ueda T, Sato Y. Unified analytical approaches for determining shear bond characteristics of FRP-concrete interfaces through pullout tests. J Adv Concr Tehnol. 2006;4(1):133–45.
[34] Ferracuti B, Savoia M, Mazzotti C. Interface law for FRP–concrete delamination. Compos Struct. 2007;80(4):523–31.
[35] Ferrier E, Quiertant M, Benzarti K, Hamelin P. Influence of the properties of externally bonded CFRP on the shear behavior of concrete/composite adhesive joints. Compos B Eng. 2010;41(5):354–62.
[36] Grande E, Imbimbo M, Sacco E. Simple model for bond behavior of masonry elements strengthened with FRP. J Compos Constr. 2011;15(3):354–63.
[37] Obaidat YT, Heyden S, Dahlblom O. Evaluation of parameters of bond action between FRP and concrete. J Compos Constr. 2013;17(5):626–35.
[38] Wu YF, Jiang C. Quantification of bond-slip relationship for externally bonded FRP-to-concrete joints. J Compos Constr. 2013;17(5):673–86.
[39] Yuan H, Wu Z, Yoshizawa H. Theoretical solutions on interfacial stress transfer of externally bonded steel/composite laminates. Doboku Gakkai Ronbunshu. 2001;2001(675):27–39.
[40] Wu Z, Yuan H, Niu H. Stress transfer and fracture propagation in different kinds of adhesive joints. J Eng Mech. 2002;128(5):562–73.
[41] Yuan H, Teng JG, Seracino R, Wu ZS, Yao J. Full-range behavior of FRP-to-concrete bonded joints. Eng Struct. 2004;26(5):553–65.
[42] Biscaia HC, Chastre C, Silva MA. Linear and nonlinear analysis of bond-slip models for interfaces between FRP composites and concrete. Compos B Eng. 2013;45(1):1554–568.
[43] Brosens K, Van, Gemert D. Plate end shear design for external CFRP laminates. Aedificatio Publishers. Fract Mech Concr Struct. 1998;3:1793–804.
[44] Teng JG, Yuan H, Chen JF. FRP-to-concrete interfaces between two adjacent cracks: theoretical model for debonding failure. Int J Solids Struct. 2006;43(18–19):5750–78.
[45] Ali MM, Oehlers DJ, Seracino R. Vertical shear interaction model between external FRP transverse plates and internal steel stirrups. Eng Struct. 2006;28(3):381–9.

[46] Ali MM, Oehlers DJ, Griffith MC, Seracino R. Interfacial stress transfer of near surface-mounted FRP-to-concrete joints. Eng Struct. 2008;30(7):1861–8.
[47] Garbin E, Panizza M, Valluzzi M. Experimental assessment of bond behaviour of fibre-reinforced polymers on brick masonry. Struc Eng Int. 2010;20(4):392–9.
[48] Kashyap J, Griffith MC, Mohamed Ali MS, Oehlers DJ. Prediction of load-slip behavior of FRP retrofitted masonry. J Compos Constr. 2011;15(6):943–51.
[49] Caggiano A, Martinelli E, Faella C. A fully-analytical approach for modelling the response of FRP plates bonded to a brittle substrate. Int J Solids Struct. 2012;49(17):2291–300.
[50] Sato Y, Kimura K, Kobatake Y. Bond behavior between CFRP sheet and concrete (Part 1). Architectural Institute of Japan. J Struct Constr Eng. 1997;62:75–82.
[51] Gao B, Leung WH, Cheung CM, Kim JK, Leung CKY. Effects of adhesive properties on strengthening of concrete beams with composite strips. Proceedings of the International Conference on FRP Composites in Civil Engineering; 2001 Dec 12–15; Hong Kong, China. Elsevier, 2001. p. 423–32.
[52] Maeda T, Komaki H, Tsubouchi K, Murakami K. Strengthening behavior of carbon fiber sheet using flexible layer. Proc Jpn Concr Inst. 2001;23(1):817–22.
[53] Nanni A, Miller B, De Lorenzis L. Bond of fiber-reinforced polymer laminates to concrete. ACI Mater J. 2001;98(3):256–64.
[54] Fernando D. Bond Behaviour and debonding failures in CFRP-strengthened steel members [dissertation]. Hong Kong: The Hong Kong Polytechnic University; 2010.
[55] Dehghani E, Daneshjoo F, Aghakouchak AA, Khaji N. A new bond-slip model for adhesive in CFRP–steel composite systems. Eng Struct. 2012;34:447–54.
[56] Yu T, Fernando D, Teng JG, Zhao XL. Experimental study on CFRP-to-steel bonded interfaces. Compos B Eng. 2012;43(5):2279–89.
[57] Fernando D, Yu T, Teng JG. Behavior of CFRP laminates bonded to a steel substrate using a ductile adhesive. J Compos Constr. 2014;18(2):04013040.
[58] Chen JF, Yuan H, Teng JG. Debonding failure along a softening FRP-to-concrete interface between two adjacent cracks in concrete members. Eng Struct. 2007;29(2):259–70.
[59] Zhou YW, Wu YF, Yun Y. Analytical modeling of the bond–slip relationship at FRP-concrete interfaces for adhesively-bonded joints. Compos B Eng. 2012;41(6):423–33.
[60] Cornetti P, Carpinteri A. Modelling the FRP-concrete delamination by means of an exponential softening law. Eng Struct. 2011;33(6):1988–2001.
[61] Liu K, Wu YF. Analytical identification of bond–slip relationship of EB-FRP joints. Compos B Eng. 2012;43(4):1955–63.
[62] Yuan H, Lu X, Hui D, Feo L. Studies on FRP-concrete interface with hardening and softening bond-slip law. Compos Struct. 2012;94(12):3781–92.
[63] Biscaia HC, Chastre C, Silva MA. Nonlinear numerical analysis of the debonding failure process of FRP-to-concrete interfaces. Compos B Eng. 2013;50:210–23.
[64] Hart-Smith LJ. Adhesive-bonded double-lap joints. NASA-CR-112236, NASA, California, USA; 1973.
[65] Volkersen O. Die Nietkraftverteilung in zugbeanspruchten Nietverbindungen mit konstanten Laschenquerschnitten. Luftfahrtfor Schung. 1938;15:41–7. (in German)
[66] Goland M, Reissner E. The stresses in cemented joints. J Appl Mech. 1944;11(1):A17–27.
[67] Rabinovitch O. Impact of thermal loads on interfacial debonding in FRP strengthened beams. Int J Solids Struct. 2010;47(24):3234–44.
[68] Wu ZS, Iwashita K, Yagashiro S, Ishikawa T, Hamaguchi Y. Temperature effect on bonding and debonding behavior between FRP sheets and concrete. J Soc. Mater Sci. 2005;54(5):474–80.
[69] Klamer E. The influence of temperature on concrete structures strengthened with externally bonded CFRP. Research Report, Eindhoven University of Technology, Eindhoven, The Netherlands; 2006.
[70] Klamer E. Influence of temperature on concrete beams strengthened in flexure with CFRP [dissertation]. Eindhoven: Eindhoven University of Technology; 2009.
[71] Leone M, Matthys S, Aiello MA. Effect of elevated service temperature on bond between FRP EBR systems and concrete. Compos B Eng. 2009;40(1):85–93.
[72] Al-Shawaf A, Al-Mahaidi R, Zhao XL. Effect of elevated temperature on bond behaviour of high modulus CFRP/steel double-strap joints. Aust J Struct Eng. 2009;10(1):63–74.
[73] Nguyen TC, Bai Y, Zhao XL, Al-Mahaidi R. Mechanical characterization of steel/CFRP double strap joints at elevated temperatures. Compos Struct. 2011;93(6):1604–12.
[74] Kim HS, Shin YS. Flexural behavior of reinforced concrete (RC) beams retrofitted with hybrid fiber reinforced polymers (FRPs) under sustaining loads. Compos Struct. 2011;93(2):802–11.
[75] Cheng L, McComb AM. Unreinforced concrete masonry walls strengthened with CFRP sheets and strips under pendulum impact. J Compos Constr. 2010;14(6):775–83.
[76] Gao WY, Teng JG, Dai JG. Effect of temperature variation on the full-range behavior of FRP-to-concrete bonded joints. J Compos Constr. 2012;16(6):671–83.
[77] Gao WY, Dai JG, Teng JG. Analysis of Mode II debonding behavior of fiber-reinforced polymer-to-substrate bonded joints subjected to combined thermal and mechanical loading. Eng Fract Mech. 2015;136:241–64.
[78] De Gennes PG. Scaling concepts in polymer physics. London, UK: Cornell University Press; 1979.
[79] Mahieux CA. A systematic stiffness-temperature model for polymers and applications to the prediction of composite behavior [dissertation]. Blacksburg (VA): Virginia Polytechnic Institute and State University; 1999.
[80] Mahieux CA, Reifsnider KL. Property modeling across transition temperatures in polymers: a robust stiffness–temperature model. Polymer. 2001;42(7):3281–91.
[81] Van Krevelen DW. Properties of polymers. 3rd ed (completely revised). Amsterdam, Oxford, New York: Elsevier Science; 1990.
[82] De Lorenzis L, Zavarise G. Modeling of mixed-mode debonding in the peel test applied to superficial reinforcements. Int J Solids Struct. 2008;45(20):5419–36.
[83] Yuan H, Wu L. Full-range behavior of FRP-to-concrete bonded joints. Eng Struct. 2004;26(5):553–65.
[84] Kafkalidis MS, Thouless MD. The effects of geometry and material properties on the fracture of single lap-shear joints. Int J Solids Struct. 2002;39(17):4367–83.
[85] Zavarise G. Problemi termomeccanici di contatto – aspetti fisici e computazionali [dissertation]. Padova: University of Padova; 1991. (in Italian)

[86] Takeo K, Matsushita H, Makizumi T, Nagashima G. Bond characteristics of CFRP sheets in the CFRP bonding technique. Proc Jpn Concr Inst. 1997;19(2):1599–604.
[87] Ueda T, Sato Y, Asano Y. Experimental study on bond strength of continuous carbon fiber sheet. Spec Publ. 1999;188:407–16.
[88] Wu Z, Yuan H, Yoshizawa H, Kanakubo T. Experimental/analytical study on interfacial fracture energy and fracture propagation along frp-concrete interface. Spec Publ. 2001;201:133–52.
[89] Tan Z. Experimental research for RC beam strengthened with GFRP [dissertation]. Beijing: Tsinghua University; 2002.
[90] Firmo JP, Correia JR, Bisby LA. Fire behaviour of FRP-strengthened reinforced concrete structural elements: A state-of-the-art review. Comp B Eng. 2015;80:198–216.
[91] Colangelo F, Russo P, Cimino F, Cioffi R, Farina I, Fraternali F, et al. Epoxy/glass fibres composites for civil applications: Comparison between thermal and microwave crosslinking routes. Comp B Eng. 2017;126:100–7.
[92] Ghosh P, Bose NR, Mitra BC, Das S. Dynamic mechanical analysis of FRP composites based on different fiber reinforcements and epoxy resin as the matrix material. J Appl Polym Sci. 1997;64(12):2467–72.